Geochemistry, Geophysics, Geosystems®

AGU ADVANCING EARTH AND SPACE SCIENCE

METHOD

10.1029/2022GC010774

Key Points:

- The Quantitative X-Ray Map Analyzer software has been used to investigate pumices and scoriae of the 2019 paroxysmal eruptions of Stromboli
- Results show evidence of small-scale hybridization by two texturally and compositionally different end-members in the final erupted tephra
- This work emphasizes the advantages of the applied procedure to obtain fast and quantitative data for complex volcanic rocks

Supporting Information:

Supporting Information may be found in the online version of this article.

Correspondence to:

M. Giuffrida,
marisa.giuffrida@unict.it

Citation:

Visalli, R., Giuffrida, M., & Viccaro, M. (2023). Unraveling textural and chemical features in volcanic rocks through advanced image processing: A case study from the 2019 paroxysmal eruptions of Stromboli. *Geochemistry, Geophysics, Geosystems*, *24*, e2022GC010774. https://doi.org/10.1029/2022GC010774

Received 18 NOV 2022
Accepted 6 FEB 2023

Unraveling Textural and Chemical Features in Volcanic Rocks Through Advanced Image Processing: A Case Study From the 2019 Paroxysmal Eruptions of Stromboli

Roberto Visalli[1], Marisa Giuffrida[1], and Marco Viccaro[1,2]

[1]Dipartimento di Scienze Biologiche Geologiche e Ambientali, Università degli Studi di Catania, Catania, Italy, [2]Istituto Nazionale di Geofisica e Vulcanologia – Sezione di Catania, Osservatorio Etneo, Catania, Italy

Abstract The Quantitative X-Ray Map Analyzer software, a new tool for image processing, has been tested on intertwined pumices and scoriae emitted during the two paroxysmal eruptions of Stromboli of 2019, whose textural and compositional heterogeneities reflect the coexistence of low porphyritic shoshonitic-basalts and high porphyritic shoshonites. The procedure applied was designed to quantitatively document the complex variations in texture and composition of these products, allowing substantial time reduction of analytical and data processing. The procedure utilizes Principal Components Analysis and supervised Maximum Likelihood Classification for multivariate statistical data handling of an array of X-ray elemental maps acquired at the millimeter scale in thin-sections. This technique permits the production of high-contrast colored images, which allow the classification of rock constituents, extrapolating the associated modal abundances and imaging chemical variations within the glass. Results highlight the close interconnection at the microscale of two types of magma in the erupted products, manifested in each processed image by the presence of contiguous areas preserving textural bulk properties typical of the pumice or scoria. The proportion of the two magmas feeding the eruptions is not simply represented by the proportions of scoria and pumice in individual clasts, as both scoria and pumice contain glass with the composition of shoshonitic-basalts and shoshonites. This method also allows the recognition of important discordances between the textural and chemical features of the two fractions involved, as well as discernment of the compositions of the two interacting magmas at the microscopic scale, even in those micro-domains showing evidence of intense interaction processes.

1. Introduction

The primary assessment of conditions related to eruption dynamics relies on the quantification and interpretation of parameters describing the spatial arrangement and mutual proportion of crystals, vesicles and glass fractions in volcanic products (Klug & Cashman, 1994; Klug et al., 2002; Polacci et al., 2018). Juvenile clasts discharged by explosive volcanic eruptions, during different phases or even within the same eruptive phase, can preserve wide textural variability at macroscopic and microscopic scale (i.e., different vesicularity, crystallinity, sizes and shapes of vesicles and crystals, extent of vesicle interconnectivity, etc.), which may reflect either variation in eruption dynamics (Gardner et al., 1998; Klug & Cashman, 1994; Klug et al., 2002; Polacci et al., 2018) or development of heterogeneous flow conditions in the conduit (Polacci, 2005; Polacci et al., 2006; Pompilio et al., 2017; Shea et al., 2012; Trafton & Giachetti, 2020).

Fast qualitative information about rock textures and the identification of rock constituents is commonly acquired using optical and electron microscopy, while more quantitative data can be obtained via image analysis techniques. The increasing use of image processing methods for studying rocks has become worthwhile for addressing geological issues in all fields of geosciences (Cossio et al., 2002; Coutelas et al., 2004; Fazio et al., 2018; Launeau et al., 1994; Leichter et al., 2022; Roda et al., 2021; Sheldrake & Higgins, 2021; Yu et al., 2023). Overall, the application of image processing for studying rocks is primarily based on a multivariate statistical analysis of EDS/WDS X-ray multispectral images that record the distribution of chemical elements (e.g., Lanari et al., 2014, 2019 and reference therein). The wide use of this analysis has also prompted the development of several GIS-based semi-automatized tools useful for identifying and classifying mineral phases, as well as quantifying modal parameters from selected thin section micro-domains (Li et al., 2008; Ortolano et al., 2018; Tarquini & Favalli, 2010; Visalli et al., 2021). In the investigation of volcanic products, image analysis has been largely applied to study vesicle and/or crystal size distributions (e.g., Gurioli et al., 2014; Neave et al., 2017;

Shea et al., 2010), as well as to emphasize compositional heterogeneities (Perugini et al., 2004; Shea et al., 2014; Yoshimura et al., 2019). However, image analysis has never been used in a semi-automated mode using GIS capabilities to investigate chemical variability within the glass portion due to magma interaction processes.

In this work, we present an efficient and straightforward strategy for acquiring textural and compositional information from volcanic samples using an ArcGIS-based external tool, the Quantitative X-Ray Map Analyzer (Q-XRMA) software (Ortolano et al., 2018). This tool allows the segmentation and classification of rock-forming constituents, highlighting potential compositional variations within the glass portion and quantifying the relative abundances starting from an array of X-ray elemental maps acquired at the thin-section microdomain scale. The methodology is tested on juvenile tephra generated during the two powerful paroxysmal eruptions that occurred at Stromboli (Aeolian Islands, Italy) on 3 July and 28 August 2019. A striking feature of the studied ejecta is the bimodal texture of individual clasts, where a poorly vesicular, high-porphyritic (HP) scoria and a highly vesicular, low-porphyritic (LP) pumice are mingled with one another (Andronico et al., 2021; Métrich et al., 2021; Pichavant et al., 2022; Viccaro et al., 2021). The coexistence of pumice and scoria is related to the extrusion of two different magmas with compositions of shoshonitic-basalt and shoshonite respectively, that are typically mingled and erupted together during violent explosive eruptions (Francalanci et al., 1999, 2004; Métrich et al., 2001, 2010). Hereafter, we will make use of the acronyms LP and HP in reference to the shoshonitic-basalts and shoshonites that produce pumices and scoriae respectively, following the traditional nomenclature and conventional use of these terms for Stromboli in the literature (Andronico & Pistolesi, 2010; Andronico et al., 2008, 2013, 2021; Bertagnini et al., 2008, 2011; Bevilacqua et al., 2020; Francalanci et al., 1999, 2004; Giordano & De Astis, 2021; Métrich et al., 2001, 2005, 2010; Pichavant et al., 2022; Polacci et al., 2009; Schiavi et al., 2010; Viccaro et al., 2021). In this contribution, we characterize these juvenile clasts via 2D image analysis using Q-XRMA on a selection of thin section micro-domains displaying the typical textural and chemical features of the LP pumice or the HP scoria.

This study highlights the potential use of Q-XRMA for fast and quantitative investigation of volcanic rocks, particularly those preserving textural and compositional complexities due to processes of chemical (mixing) and/or mechanical (mingling) magmatic interaction. We show that the new image analysis approach proposed here can be used to uncover even subtle compositional variations that are often concealed at the microscopic scale due to the intense degree of magma hybridization. We do not attempt statistical characterization of the variation in the clast textures to develop a model of magma ascent, vesiculation, and fragmentation upon eruption. Rather, we propose the application of a new reliable, semi-automatic quantification method allowing users to easily catalog features of volcanic clasts and characterize their chemistry.

As a first step, the software is applied for the definition of the modal abundances of crystals, vesicles, and glasses in selected micro-domains within the pumice and scoria portions. Next, we focus on the compositional variability of glasses to quantitatively discern between LP and HP magmas in individual domains and the relative proportion of these two magmas in the studied tephra. This study illustrates the need for a generalized procedure able to rapidly capture and quantify the parameters essential to understanding magma interaction processes. This tool will be of immense value to petrologists and volcanologists for gathering in-depth information regarding physical and chemical volcanic processes.

2. Methods

The present work focuses on 17 air-quenched clasts emplaced during the two paroxysms at Stromboli on 3 July and 28 August 2019. The analyzed clasts were selected carefully based on their mingling structures (i.e., pumice/scoria pairs), making them suitable for the purpose of this study, which is a demonstration of the method. The main characteristics of the investigated fragments are detailed in the next section. Thin and polished, 80 μm-thick sections were made for individual fragments for petrographic, micro-chemical and image analyses. Twenty-eight representative micro-domains from distinct samples associated with the two 2019 paroxysmal episodes were selected at the scale of thin sections for quantitative textural analyses by Q-XRMA. For each paroxysmal eruption considered, we analyzed fourteen micro-domains. Seven were chosen as representative of the HP scoria, while seven were selected as typical of the LP pumice, in accordance with their bulk textural properties. Selection and classification of micro-domains were done by taking into account the main differences in vesicle and crystal abundances, sizes and overall distributions. The availability of previous textural information (Viccaro et al., 2021, and references therein) was helpful for the initial classification of textural domains as a representative

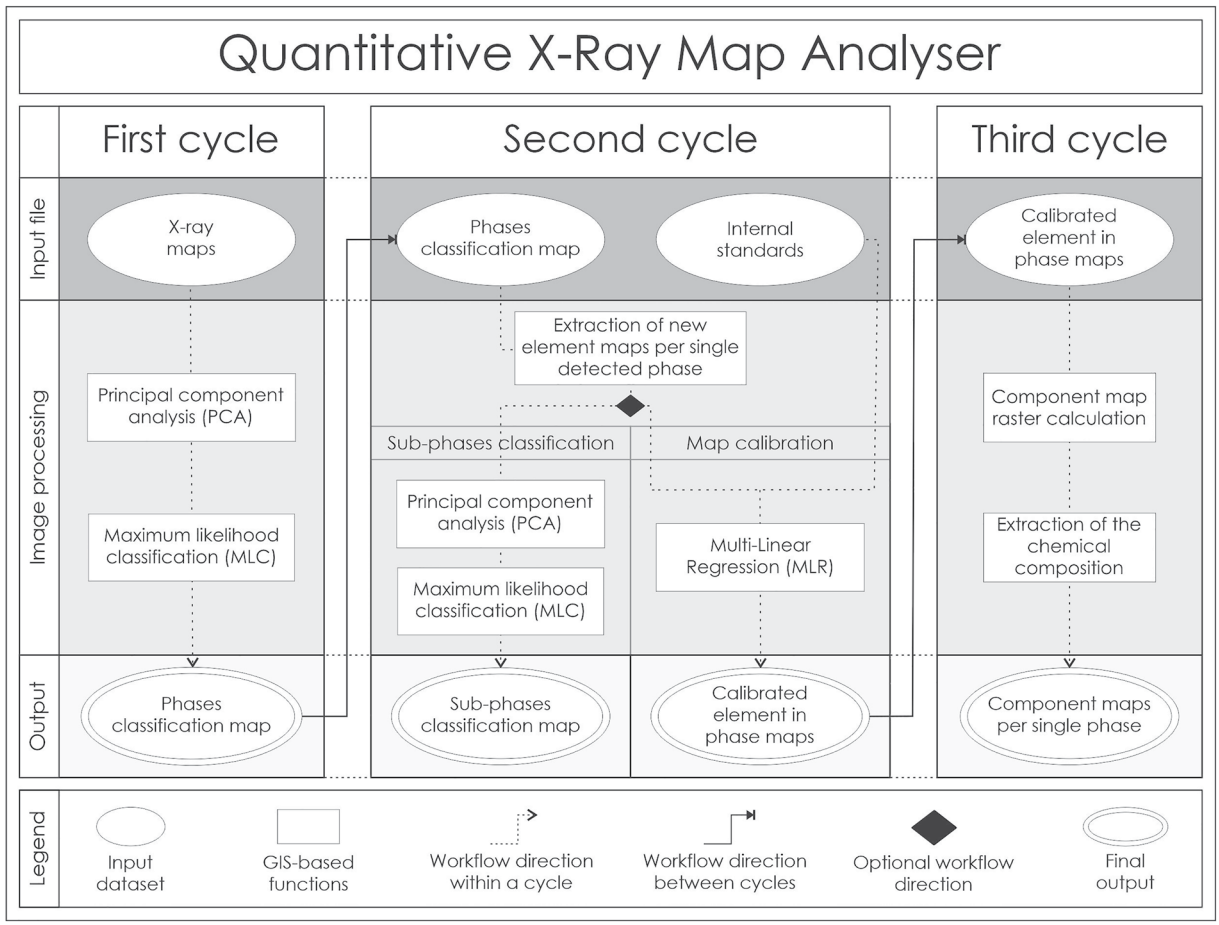

Figure 1. Simplified flow chart of the Quantitative X-Ray Map Analyzer workflow (modified after Ortolano et al. (2018)).

of the scoria or pumice fractions. Specifically, main criteria adopted for discriminating micro-domains of the pumice type from those of the scoria type include: (a) the characteristic of groundmass, which is almost exclusively glassy or contains just few micro-phenocrysts (<200 μm) in pumices, while it is highly crystallized in scoriae; (b) the degree of vesicularity that is higher than 50% in pumice, though it can be highly variable in scoria (e.g., Pioli et al., 2014; Polacci et al., 2009) as determined by optical and electronic microscope inspections; and (c) the variance in bubble size and shapes, with the pumice domains distinguished for the abundance of small vesicles that are mostly rounded or slightly elongated. Further details on the bulk textural properties of pumice and scoria in the studied samples are provided in Section 3 of this study.

X-ray maps were acquired for each domain (Figures S1–S7 in Supporting Information S1) to derive the distribution and concentration of the elements Al, Ca, Cl, Fe, K, Mg, Mn, Na, P, Si, and Ti. Energy-dispersive X-ray spectroscopy, EDAX Neptune XM460 series, assembled on a TESCAN VEGA LMU scanning electron microscope (SEM) at the Department of Biological, Geological and Environmental Sciences, University of Catania, was used to acquire X-ray maps under high vacuum conditions at an accelerating voltage of 20 kV, beam current of 8 nA and working distance of 15.5 mm. The resolution of the output images is 512 × 400 pixels for an average pixel size of 4 μm in 256 grey-scale levels (i.e., eight-bit images) obtained with a dwell time of 500 μs per 128 frames, consistent with an acquisition time for each map of 4 hr and 30 min.

X-ray maps were processed through the Q-XRMA software (Ortolano et al., 2018) to recognize the rock constituents and to extrapolate quantitatively the associated modal abundances, as well as to investigate the occurrence of potential compositional variations within the glass portion to be linked with magma interaction processes (mingling vs. mixing). The total time for the processing of each X-ray map array is on the order of 30–60 min.

Overall, the entire Q-XRMA procedure provides users with three different analytical cycles (Figure 1). The first cycle is based on a multivariate statistical data handling of the X-ray raster maps (e.g., Figure 2a) by adopting

the Principal Components Analysis (PCA; Hotelling, 1933; Jolliffe, 2002; Karl Pearson, 1901) and the supervised Maximum Likelihood Classification (MLC; Johnson & Wichern, 1988; Ortolano et al., 2014; Richards & Jia, 2006), with the aims of identifying the rock-forming phases at thin section and microdomain scales, as well as quantifying the associated modal percentage. PCA is a statistical technique used for simplifying a data set with the aim of synthesizing the information provided by the variables of the data set into new variables called principal components (PCs) while preserving as much of the relevant information as possible. Therefore, the main goal of this technique is to maximize the variance of these components by calculating the weight to be attributed to each starting variable in order to reduce the dimensionality of the starting multivariate data. In the Q-XRMA, this technique allows the compression of data by eliminating redundancy, emphasizing the variance within the bands of a raster, and making the data more interpretable. Such a procedure can aid the operator in recognizing the potential inter-dependence between the elemental variability linked with the recognition of the rock constituents. This is achieved through a linear transformation of the data attributes of an original multiband raster, such as the X-ray map array, to a new attribute space where the new set of bands (i.e., the PC maps) are linear functions of the original bands. The result of this transformation is a new multiband raster (e.g., Figure 2b) with the same number of bands as the original raster, where the PCs are sorted in descending order of variance. This is accomplished by calculating the covariance matrix for the entire data set and then sorting the eigenvectors (columns) and eigenvalues (rows) of the covariance matrix by the decreasing eigenvalue (Table 1). Each eigenvalue is expressed as a percentage of the total, highlighting which PC is more informative for distinguishing minerals, whereas the eigenvectors represent the new axes of the multidimensional space. These latter are expressed as vectors oriented with respect to the previous primary elemental maps and allow recognizing the rock-forming phases by the user through the pixel brightness of the PC maps (e.g., Figure 2b) as a function of the eigenvector orientation values (from −1, pure black, to 1, pure white).

The MLC allows grouping the pixels of a raster into classes (for a supervised classification) or clusters (for an unsupervised classification) by using the statistical distribution of the 0–255 greyscale attribute values in order to assign to single pixels a probability degree of belonging to a specific class or cluster (Figure 2c). With this aim, a spectral signature file containing a subset of pixels, from the PC maps and representative of a specific class or cluster, is required. Such a signature file includes the mean, the number of cells, and the variance-covariance matrix for the class or cluster, and it can be created through an unsupervised or a supervised approach. In the unsupervised approach, the Q-XRMA performs an automatic classification through multivariate statistics computation by aggregating pixels into a number of clusters specified by the user. The supervised classification provides the user interaction via the creation of some training areas enclosing those pixels representative of each class through the ArcGIS interface on the PCA multiband raster. In both approaches, it is possible to define the a priori probability of a pixel being assigned to a specific class or cluster between two choices: (a) Equal, where each pixel is assigned to the class to which it has the highest likelihood of being a member, or (b) Sample, where the likelihood of a pixel of being part of a class or cluster is proportional to the number of representative pixels captured in each signature. As a result, a classified map that partitions the study area into known classes (supervised approach) or naturally occurring clusters (unsupervised approach) is obtained, and the associated modal abundances are calculated on the total of the map pixel matrix. Finally, post-classification filters operating in a 3×3 pixel matrix (i.e., focal median and maximum frequency) can be applied to the classified image to minimize the effect of misclassified pixels.

The second cycle allows performing in-depth analysis on a specific class identified in the first cycle by creating, via map algebra operations (Dainelli et al., 2010), new elemental maps per single detected class (e.g., Figure 3a) at the beginning of the cycle. This step is crucial to highlight better, with respect to the original x-ray maps, the potential occurrence of chemical variability within a class. This cycle provides two distinct analytical routines. The first one consists of a sub-classification procedure of the selected class to detect the presence of compositional patterns through the application of the PCA and MLC algorithms (Figures 3b and 3c). In this case, the user can choose whether to include all elements for executing the PCA or only the elements considered useful in describing the chemical variability for the selected class. The second routine permits the calibration of the X-ray maps by applying a multiple linear regression algorithm on the base of several spot analyses used as internal standards. Finally, the third cycle allows creating end-member maps of a specific class by using the calibrated maps.

In this work, the first cycle has been applied to identify vesicles, crystals, and glass portions and derive the related modal abundances in the investigated microdomains, whereas only the first routine of the second cycle has been

10.1029/2022GC010774

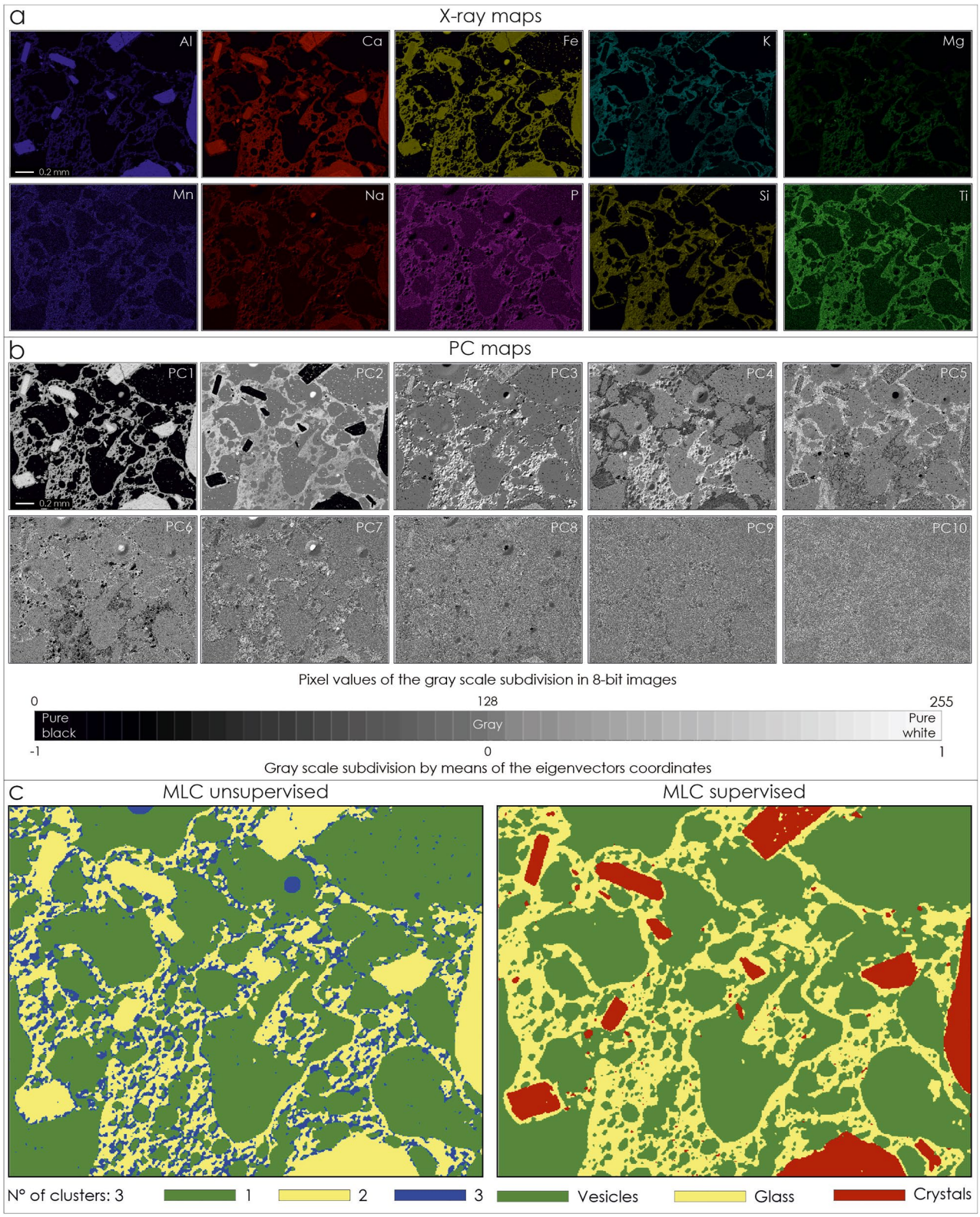

Figure 2. Example of the Quantitative X-Ray Map Analyzer first cycle procedure from the input image to the classified images: (a) example of an X-ray map array; (b) an example of the principal component maps obtained through the Principal Components Analysis; and (c) an example of classified images obtained via an unsupervised approach by selecting three clusters and a supervised one.

Geochemistry, Geophysics, Geosystems

10.1029/2022GC010774

Table 1
Example of Calculated Eigenvectors and Eigenvalues Through the Principal Components Analysis With Relative Elemental and Phase Recognition Per Eigenvector

Principal component	1st	2nd	3rd	4th	5th	6th	7th	8th	9th	10th
Eigenvalues	3,448.15	250.29	85.89	50.58	27.76	18.10	11.95	9.17	3.85	2.12
Eigenvalues %	88.24	6.40	2.20	1.29	0.71	0.46	0.31	0.23	0.10	0.05
Element	Eigenvectors									
Al	0.61	−0.73	−0.18	0.18	−0.15	0.06	−0.06	−0.01	0.01	0.00
Ca	0.32	−0.06	0.79	−0.08	0.49	0.00	0.17	0.01	−0.02	−0.02
Fe	0.07	0.16	0.38	0.15	−0.41	0.36	−0.62	0.34	−0.08	−0.04
K	0.09	0.15	0.15	0.08	−0.46	0.50	0.58	−0.36	−0.11	−0.01
Mg	0.15	0.31	−0.06	0.90	0.18	−0.16	0.00	−0.12	0.00	0.00
Mn	0.01	0.01	0.04	0.00	−0.02	0.02	−0.01	0.01	0.03	1.00
Na	0.11	0.12	−0.34	−0.07	0.55	0.72	−0.18	−0.07	0.01	0.00
P	0.05	0.05	−0.14	0.09	0.03	0.11	0.47	0.86	−0.02	0.00
Si	0.69	0.54	−0.19	−0.34	−0.12	−0.25	−0.04	−0.01	−0.01	0.00
Ti	0.02	0.04	0.06	0.02	−0.08	0.08	0.03	0.01	0.99	−0.04
Elemental brightness in PC maps	Si-Al-Ca-Mg-Na-K-Fe-P-Ti-Mn	Si-Mg-Fe-K-Na-P-Ti-Mn	Ca-Fe-K-Ti-Mn	Mg-Al-Fe-P-K-Ti	Na-Ca-Mg-P	Na-K-Fe-P-Ti-Al-Mn	K-P-Ca-Ti	P-Fe-Ca-Mn-Ti	Ti-Mn-Al-Na	Mn
Phase recognition by the user[a]	Gl-Cr	Vs-Gl	Vs-Gl-Cr	Vs-Gl	Vs-Cr	Vs-Gl	Vs-Gl-Bk	Bk	Bk	Bk

[a]Legend: Vs—Vesicles; Gl—Glass; Cr—Crystals; and Bk—Background.

10.1029/2022GC010774

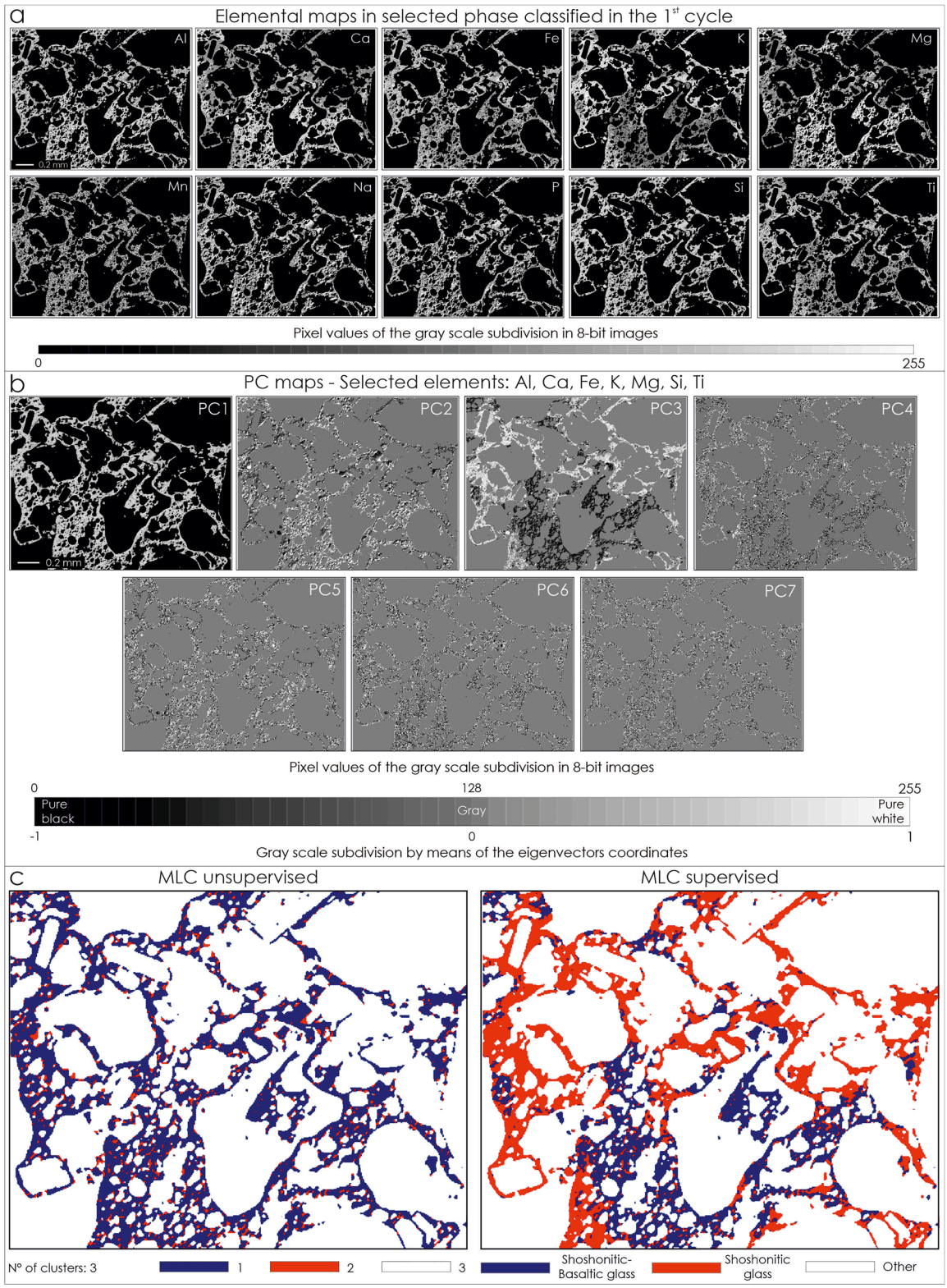

Figure 3. Example of the Quantitative X-Ray Map Analyzer second cycle procedure from the input image to the classified images: (a) example of the new elemental maps per single phase obtained at the beginning of the cycle; (b) an example of the principal component maps obtained through the Principal Components Analysis for the selected phase; and (c) an example of classified images obtained via an unsupervised approach by selecting three clusters and a supervised one.

used, focusing the investigation on the glass portion. The first six PC maps have been selected as most informative in the first cycle for all of the analyzed microdomains, while the first three or four PCA maps have been chosen in the second cycle by taking into account Al, Ca, Fe, K, Mg, Si, and Ti as the elements of interest. The supervised classification has been adopted in both analytical cycles by choosing the Sample a priori probability, whereas the maximum frequency filter has been applied in the post-classification phase.

The second cycle has produced high-contrast images useful for discerning between chemically homogeneous zones based on the contrast in color. This step required an appropriate number of spot analyses to verify the geochemical affinity of different colored glass zones with the composition of the HP shoshonite or LP shoshonitic-basalt, respectively. This checking procedure was performed on two different micro-domains associated with distinct eruptive episodes. All measurements were done at the University of Catania by scanning electron microscopy, using the same instrumentation described above. Operating conditions were set at 20 kV accelerating voltage with 2 Na beam current to obtain the analysis of major element abundances. Repeated analyses on SIP 02753-AB Serial KEF certified standard glass during the analytical runs provided precision for all measured elements of around 3%–5%.

3. Volcanological Background and Sample Description

Stromboli, the northernmost volcano of the Elian Archipelago (Southern Italy), is famous for its persistent volcanic activity consisting of continuous active degassing associated with intermittent low-energy explosions (generally 3–6 events/hr) characterized by the emission of a poorly vesicular, crystal-rich scoria of shoshonitic composition (Rosi et al., 2000, 2013). This steady-state activity is periodically interrupted by major explosions (also called small-scale paroxysms; Barberi et al., 1993; Bertagnini et al., 2008), which occur with a frequency of ∼1–3 times/year (Bevilacqua et al., 2020, and references therein). Large-scale paroxysms (or paroxysms for simplicity; Bertagnini et al., 2011) are the least frequent, yet the most violent, eruptive manifestations at Stromboli (Barberi et al., 1993; Métrich et al., 2005). They typically consist of powerful, short-lasting explosions producing eruptive columns 3–5 km high and ejecting pyroclastic material a few kilometers from the crater terrace. Based on historical records, large-scale paroxysms are rare, occurring with a frequency of 5–10 years (Barberi et al., 1993; Bevilacqua et al., 2020; Francalanci et al., 1999, 2004).

Unlike the ordinary activity, major explosions and paroxysms are distinguished for the concomitant emission of dark scoriae and light pumices, the latter being highly vesicular and crystal poor (<10 vol.% of crystals; Francalanci et al., 1999, 2004; Métrich et al., 2001, 2010). These two fractions originate from two distinct, physically and chemically constrained magmas that are often mingled upon eruption. The scoria originates from a nearly degassed, HP magma of shoshonitic composition (e.g., Corsaro et al., 2005; Francalanci et al., 1999, 2004) that resides in the shallow (2–4 km below the summit) plumbing system. The pumice (conventionally called "golden pumice" for the yellowish color) is associated with the rise of a more primitive (high-K to shoshonitic basaltic), volatile-rich, and LP magma coming from depths of ∼7–10 km (Francalanci et al., 2004; Métrich et al., 2001, 2010). The emission of LP magma mingled with the HP one has been documented for a range of recent eruptive episodes at Stromboli (e.g., the 2003, 2005, 2007 and 2009 paroxysmal eruptions; Andronico & Pistolesi, 2010; Andronico et al., 2008, 2013; Pioli et al., 2014; Polacci et al., 2009; Schiavi et al., 2010), including those of the summer 2019 (Andronico et al., 2021; Giordano & De Astis, 2021; Pichavant et al., 2022; Viccaro et al., 2021).

The paroxysmal eruptions of 3 July and 28 August 2019 took place in a period of moderate, normal activity at Stromboli and they were not preceded by significant changes in the routinely monitored geophysical parameters (Giudicepietro et al., 2020). The first paroxysm occurred in the early afternoon of 3 July in a sequence of two short-lasting explosions that rapidly evolved in a >6 km-high eruptive column. The partial collapse of the convective column generated two pyroclastic density currents, which in turn triggered a small tsunami as they reached the sea. After 3 July, the summit activity remained at high levels for almost 2 months, with intense Strombolian explosions accompanied by the emission of small lava flows from the summit craters. The second paroxysm, on 28 August, mostly reproduced the same sequence of events registered during the 3 July paroxysm, but it consisted of three main explosions. The first explosion was the most powerful and produced an eruptive column rising up to ∼6 km, consistent with that of the 3 July paroxysm (Andronico et al., 2021; Giudicepietro et al., 2020). The output of lava definitively ceased on 31 August, while the summit Strombolian activity persisted at a high level until the second half of the September 2019. Both eruptions produced abundant tephra fallout of shosho-

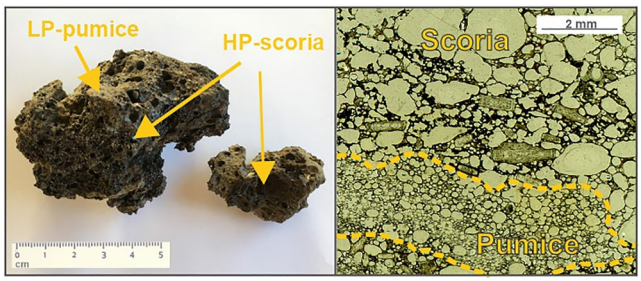

Figure 4. (a) Selected tephra from the paroxysm of 3 July 2019; and (b) optical microscope image taken under plane polarizing light for a representative tephra of 3 July 2019, illustrating the coexistence of low-porphyritic (LP) pumice and high-porphyritic (HP) scoria within the same sample.

nitic (53–55 wt.% SiO_2; >3.5 wt.% K_2O) to shoshonitic-basaltic composition (49–52 wt.% SiO_2; <2.7 wt.% K_2O), which typically reflects syn-eruptive mingling between the two magmatic endmembers (Andronico et al., 2021; Giordano & De Astis, 2021; Viccaro et al., 2021).

For the present study, we investigated a population of pyroclastic material (each clast 2–7 cm across the longest axis) that was collected immediately after the end of the eruptions of 3 July and 28 August 2019 at different sites close to the village of Ginostra, on the western side of the island, at a distance of 2–3 km from the crater terrace (Figure 4a). The studied samples derive from the collection of Viccaro et al. (2021). The petrology and geochemistry of these samples have been extensively discussed by various authors (Andronico et al., 2021; Pichavant et al., 2022; Viccaro et al., 2021), who did not find significant differences between major element compositions of clasts erupted on 3 July compared to 28 August. Accordingly, we provide here a common description of the products of the two eruptions. Samples are nearly aphyric pumices characterized by significant scoriaceous portions that are crystal-rich and contain large vesicles, with vesicle size orders of magnitude higher than in pumice. Because of the coexistence of pumice and scoria, individual clasts are texturally and chemically heterogeneous at the scale of a single thin section, exhibiting major variability in bulk properties such as vesicularity (up to 80 vol.%) and crystallinity (5–55 vol. %) in accordance with previous petrological observations (e.g., Polacci et al., 2009; Pioli et al., 2014; Figure 4b). A first qualitative assessment of these properties has been provided using a combination of optical microscopy and high-resolution backscattered electron images, as described in the method section of this study. The pumice fraction is overall aphyric with crystal content lower than 5%–10% by volume. The pumice glasses are characterized by a dense network of μm-sized, rounded to slightly elongated vesicles coalescing at microscopic scale. The scoria fraction is highly crystallized, with crystal content of about 45%–50% by volume. Vesicles are large (up to several mm in size) and mostly composed of single, convoluted blobs that appear to be produced by extensive coalescence of smaller vesicles. The two fractions show the same paragenesis consisting of plagioclase, olivine and clinopyroxene, although the relative abundance of mineral phases is quite different between pumice and scoria. Scoria contains crystals of olivine (5–10 vol% of the total mineral assemblage), clinopyroxene (15–35 vol%), and plagioclase (50–75 vol%). Pumice has higher abundances of olivine (10–20 vol%) and clinopyroxene (45%–72%) with respect to plagioclase (<10%), and crystals have smaller sizes (usually <200 μm) than those of scoria, with a large prevalence of micro-phenocrysts.

4. Results

The first cycle of Q-XRMA allows the recognition of vesicles, crystals and glass for selected micro-domains, as well as the associated modal percentage to be calculated (Figures 5–7, Figures S8–S11 in Supporting Information S1). Results are synthesized in Table 2 for volcanic samples related to the paroxysmal eruptions of 3 July and 28 August 2019, which contain both scoria and pumice domains. Fragments discharged during the episode of 3 July show, on average, lower modal abundances of crystals (4.7% ± 6.4%) and vesicles (66.9% ± 9.5%), but higher glass fraction (28.4% ± 10.4%) than fragments discharged during the episode of 28 August (5.9% ± 6.5% crystals, 70.2% ± 9.3% vesicles, and 23.9% ± 8.1% glass; Figure 5; Table 2). More prominent differences emerged from the elaboration of data for the same eruptive episode as the pumice and scoria domains were compared.

The application of the first cycle on products related to the 3 July 2019 eruption indicates total vesicularity in the range 50.0%–81.2% (Figure 5, Table 2). In these products, the scoria domains record an average vesicle modal percentage that is 6.0% higher than in pumice (Table 2). The total crystallinity varies from zero to 22.3%, but reduces dramatically from scoria (8.5% ± 7.3% on average) to pumice (0.9% ± 1.1%). In contrast, the glass fraction increases from a mean value of 21.4% ± 5.0% in scoria to 35.4% ± 9.7% in pumice domains, reaching a maximum absolute value of 48.7% (Table 2).

Fragments erupted on 28 August characterize for total vesicularity of 53.3%–84.4%, crystallinity of 0.2%–24.8%, and a glass fraction that varies from 10.6% to 38.2% (Figure 5, Table 2). The pumice and scoria domains of 28 August do not differ significantly in terms of vesicle percentage (68.5% ± 7.5% for pumice vs. 72.0% ± 11.2% for scoria). Instead, there exists a marked difference in both crystal content and glass fraction. The former

reduces from 9.0% ± 8.0% in scoria to 2.7% ± 2.2% in pumice, while the latter increases from 19.0% ± 7.0 to 28.8% ± 6.0% for the same domains (Figure 5, Table 2).

The second cycle of the Q-XRMA quantifies the chemical variability of matrix glasses, including discerning between the glass fractions with a composition typical of the shoshonitic HP magma and fractions chemically akin to the LP shoshonitic-basaltic magma of Stromboli. Figures 8 and 9 show the spatial distribution of the two glass compositions in individual domains for both paroxysmal events (see also Figures S10 and S11 in Supporting Information S1). According to our results (Figure 5, Table 3), the shoshonitic-basaltic glasses dominate in all the selected domains for the eruption of 3 July (72.3% ± 32.4%) and the 28 August episode (62.1% ± 32.8%). Yet, the shoshonitic glasses are overall more abundant in domains of 28 August (37.9% ± 32.8%) than those of July (27.7% ± 32.4%). When comparing the compositional diversity of pumice and scoria from both eruptions, we found an elevated percentage (>62%) of shoshonitic-basaltic glass in the domains that texturally resemble the LP pumice typically erupted at Stromboli during extraordinary explosive episodes. By contrast, some domains that have been originally classified as scoria-like ones, based on their textural features, preserve the typical shoshonitic-basaltic composition of the LP pumices of Stromboli (Table 3). Such discordance between textural and chemical features is well evident in three domains related to the eruption of 3 July (J_ST4_1, J_ST11_1, and J_ST18_2) and in two of 28 August (A_ST3_1 and A_ST8_1), all preserving an abundant glass fraction of shoshonitic-basaltic composition in percentages higher than 74%.

5. Discussion

Quantitative observations of juvenile tephra from the 3 July and 28 August 2019 paroxysmal eruptions of Stromboli highlighted the large variability of products both within single and among different eruptive episodes. Major differences among the studied samples pertain to composition, crystallinity and vesicularity, whose dissimilarities extend at the scale of the single micro-domains. Such observations in terms of textural and chemical complexities overlap those of previous paroxysmal eruptions at Stromboli (Landi et al., 2009; Pichavant et al., 2011; Pioli et al., 2014; Polacci et al., 2006, 2009; Schiavi et al., 2010), and reflect the interaction between two compositionally

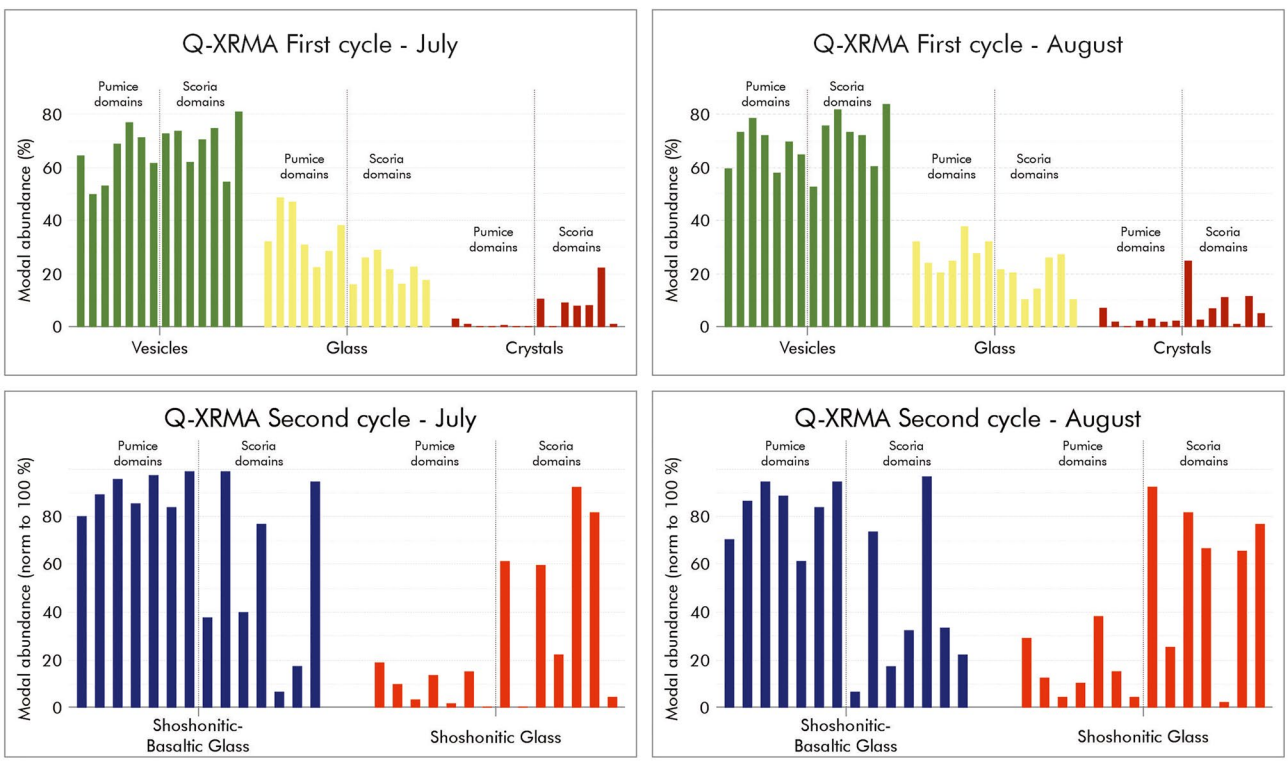

Figure 5. Modal abundances obtained using Quantitative X-Ray Map Analyzer on rock constituents (First cycle, up left and right) and the glass fraction (Second cycle, down left and right) for the micro-domains in product representative of the 3 July and 28 August paroxysms.

Table 2
Modal Percentages of Vesicles, Glass, and Crystals Obtained From the First Cycle of the Quantitative X-Ray Map Analyzer (Q-XRMA) on Selected Pumice and Scoria Micro-Domains Related to the Stromboli Eruptions of 3 July and 28 August 2019

	Q-XRMA first cycle—JULY					Q-XRMA first cycle—AUGUST			
Micro-domain	Vesicles %	Glass %	Crystals %	Type	Micro-domain	Vesicles %	Glass %	Crystals %	Type
J_ST3_1	64.6	32.2	3.2	PUMICE	A_ST1_1	60.3	32.4	7.3	PUMICE
J_ST3_2	50.0	48.7	1.3	PUMICE	A_ST3_2	73.8	24.4	1.8	PUMICE
J_ST4_2	53.0	47.0	0.0	PUMICE	A_ST4_1	79.1	20.7	0.2	PUMICE
J_ST5_1	68.9	30.8	0.3	PUMICE	A_ST5_2	72.5	25.3	2.2	PUMICE
J_ST11_2	76.9	22.3	0.7	PUMICE	A_ST9_1	58.5	38.2	3.2	PUMICE
J_ST13_1	71.3	28.6	0.2	PUMICE	A_ST10_1	70.1	28.0	1.9	PUMICE
J_ST18_1	61.5	38.2	0.4	PUMICE	A_ST10_2	65.3	32.5	2.3	PUMICE
J_ST1_2	73.2	15.9	10.8	SCORIA	A_ST2_1	53.3	21.9	24.8	SCORIA
J_ST4_1	73.7	26.2	0.0	SCORIA	A_ST3_1	76.4	20.9	2.7	SCORIA
J_ST7_2	62.2	28.8	9.0	SCORIA	A_ST4_2	82.3	10.7	6.9	SCORIA
J_ST11_1	70.3	21.7	7.9	SCORIA	A_ST5_1	73.8	14.8	11.4	SCORIA
J_ST12_1	75.2	16.5	8.4	SCORIA	A_ST8_1	72.6	26.5	0.9	SCORIA
J_ST12_2	54.8	22.9	22.3	SCORIA	A_ST8_2	61.0	27.5	11.4	SCORIA
J_ST18_2	81.2	17.6	1.2	SCORIA	A_ST9_2	84.4	10.6	5.0	SCORIA
Mean total	66.9	28.4	4.7		Mean total	70.2	23.9	5.9	
St.Dv	9.5	10.4	6.4		St.Dv	9.3	8.1	6.5	
Mean pumice	63.7	35.4	0.9		Mean pumice	68.5	28.8	2.7	
St.Dv	9.7	9.7	1.1		St.Dv	7.5	6.0	2.2	
Mean scoria	70.1	21.4	8.5		Mean scoria	72.0	19.0	9.0	
St.Dv	8.8	5.0	7.3		St.Dv	11.2	7.0	8.0	

and physically distinct magmas, one producing the LP pumices (i.e., the LP shoshonitic-basaltic magma) and one producing the HP, dark scoriae (i.e., the HP shoshonitic magma). Since these two magmas are associated with different storage conditions and eruptive dynamics, the analysis of textural and compositional complexities of the fall-out material may greatly contribute to understand their mutual relationships and the potential variations developed into the feeding system during the time lapse between the two events.

The strength of the applied methodology lies in its capability to identify and quantify chemical heterogeneities at the microscopic scale. Similar studies focused on unraveling the textural and chemical complexities of tephra erupted during the 2019 Stromboli paroxysms were carried out by Pichavant et al. (2022), who used a combination of X-ray mapping and X-ray computed microtomography to characterize mixed samples that include portions representative of both LP and HP magmas. Their analyses of X-ray distribution map underline the strong compositional contrast between the two components, which is evident in the zones where the chemical transition from one glass to the other appears sharp at the mm scale. However, the HP-LP transition is revealed to be chemically and texturally more complex at the micrometric scale (<50 μm, Andronico et al., 2021; Pichavant et al., 2022; Viccaro et al., 2021), which requires more in-depth characterization and quantification using high-resolution micro-analytical approaches. Our analyses dramatically emphasize the coexistence and pervasive interconnection of pumice and scoria, evident in each processed image, albeit in variable proportions (Figures 6–9). These features were evident even within those micro-domains that appear to be texturally homogeneous through SEM observations (e.g., Viccaro et al., 2021).

Comparisons among representative images for each micro-domain (Figures 6 and 7, Figures S8 and S9 in Supporting Information S1) clearly show the presence of contiguous areas preserving bulk properties that are typical of the light pumice or the dark scoria, respectively. Pumice and scoria are distinguishable in terms of degree of crystallization, vesicle size, abundance and interconnectivity, as well as percentage of glass. Thus, the

Table 3
Modal Percentages of the Glass Sub-Phases Obtained From the Second Cycle of the Quantitative X-Ray Map Analyzer (Q-XRMA) on Selected Pumice and Scoria Micro-Domains Related to the Stromboli Eruptions of 3 July and 28 August 2019

Micro-domain	Shoshonitic-basaltic glass %	Shoshonitic glass %	Shoshonitic-basaltic glass normalized to 100%	Shoshonitic glass normalized to 100%	Type
Q-XRMA Second cycle—JULY					
J_ST3_1	25.9	6.1	81.0	19.0	PUMICE
J_ST3_2	44.2	4.9	89.9	10.1	PUMICE
J_ST4_2	44.9	1.5	96.8	3.2	PUMICE
J_ST5_1	25.7	4.1	86.3	13.7	PUMICE
J_ST11_2	21.7	0.3	98.4	1.5	PUMICE
J_ST13_1	23.5	4.2	84.9	15.1	PUMICE
J_ST18_1	38.2	0.0	100.0	0.0	PUMICE
J_ST1_2	5.8	9.4	38.2	61.7	SCORIA
J_ST4_1	26.2	0.0	100.0	0.0	SCORIA
J_ST7_2	11.3	17.0	40.0	60.0	SCORIA
J_ST11_1	16.4	4.8	77.5	22.5	SCORIA
J_ST12_1	1.0	14.8	6.5	93.5	SCORIA
J_ST12_2	3.8	18.3	17.3	82.7	SCORIA
J_ST18_2	16.4	0.8	95.6	4.4	SCORIA
Mean total	21.8	6.2	72.3	27.7	
St.Dv	14.0	6.3	32.4	32.4	
Mean pumice	32.0	3.0	91.0	8.9	
St.Dv	10.1	2.4	7.4	7.4	
Mean scoria	11.6	9.3	53.6	46.4	
St.Dv	8.8	7.6	37.5	37.5	
Q-XRMA Second cycle—AUGUST					
A_ST1_1	22.5	9.2	70.9	29.1	PUMICE
A_ST3_2	20.4	2.9	87.5	12.5	PUMICE
A_ST4_1	19.1	0.9	95.4	4.6	PUMICE
A_ST5_2	22.3	2.6	89.6	10.4	PUMICE
A_ST9_1	23.2	14.4	61.7	38.3	PUMICE
A_ST10_1	23.3	4.3	84.5	15.5	PUMICE
A_ST10_2	30.2	1.4	95.5	4.5	PUMICE
A_ST2_1	1.4	19.7	6.5	93.5	SCORIA
A_ST3_1	14.7	5.1	74.2	25.8	SCORIA
A_ST4_2	1.7	8.2	17.5	82.5	SCORIA
A_ST5_1	4.5	9.5	32.4	67.6	SCORIA
A_ST8_1	25.6	0.6	97.8	2.1	SCORIA
A_ST8_2	9.2	17.9	33.9	66.1	SCORIA
A_ST9_2	2.2	7.7	22.5	77.5	SCORIA
Mean total	15.7	7.4	62.1	37.9	
St.Dv	10.0	6.2	32.8	32.8	
Mean pumice	23.0	5.1	83.6	16.4	

Table 3
Continued

Micro-domain	Shoshonitic-basaltic glass %	Shoshonitic glass %	Shoshonitic-basaltic glass normalized to 100%	Shoshonitic glass normalized to 100%	Type
St.Dv	3.5	4.9	12.7	12.7	
Mean scoria	8.5	9.8	40.7	59.3	
St.Dv	9.0	6.8	33.0	33.0	

quantification of total abundances of crystals, vesicles and glasses for each classified micro-domain gives us indications on the actual proportions of the LP and HP magmas involved in the interaction process.

The examination of the modal abundances of crystals, vesicles and glasses for clasts of different eruptive episodes tells us that fragments from the 28 August paroxysm turned out to contain larger proportions of vesicles and crystals, but lower glass fraction than fragments from 3 July, features suggesting a dominant scoriaceous fraction. The pumice-like domains of 28 August were also distinguished for higher vesicle and crystal percentage than the July pumice domains, and the same is observed comparing the scoria-like domains of the two episodes (Figure 5, Table 2).

Extensive mixing between LP and HP magmas is also demonstrated by the chemical heterogeneity of the glassy matrix in the products of both paroxysmal eruptions. The compositional information obtained by Q-XRMA matched the qualitative observations derived from elemental X-ray maps; however, the chemical resolution achievable at the microscopic scale is much higher. The high resolution achieved allowed clear characterization of the degree of magma hybridization, as well as quantification of the modal abundances of the two magmas involved in the interaction process during both eruptions. The interaction between the two types of magma is shown clearly in all processed images via the contrast in color, which is due to the chemical contrast (Figures 8 and 9, Figures S3 and S4 in Supporting Information S1). Validation of these results comes from the micro-analytical inspection of the matrix glass that allowed the basaltic and shoshonitic compositions to be ascribed to specific colored areas, blue and red respectively (Figure 10, Table S1 in Supporting Information S1).

Results indicate that the shoshonitic glass (3.8–4.5 wt.% K_2O) is overall more widespread in fragments erupted during the August paroxysms relative to those erupted in July, with a difference of 13% by area. Thus, textural and compositional observations lead to mechanisms of syn-eruptive mingling and mixing where the fraction of shoshonitic-basaltic liquid erupted on 28 August was smaller than that erupted on 3 July. Our work therefore emphasizes that subtle textural and compositional differences exist, even though juvenile fragments erupted during both paroxysms share similar petrological characteristics and result from comparable processes of disequilibrium degassing, and similar magnitudes and intensities of the eruption (Andronico et al., 2021; Giordano & De Astis, 2021; Pichavant et al., 2022; Viccaro et al., 2021).

6. Concluding Remarks

The advanced image processing procedure presented in this study provides fast, quantitative data for volcanic rocks showing textural and chemical complexity at the microscopic scale as a result of mechanical and/or chemical magmatic interactions. In many cases, there is clear macro- to microscopic evidence for magma interaction, where the involved end-members have lost their physical identities to some extent, depending on the degree of hybridization. In such circumstances, it may be challenging to separate physically coexisting fractions, unless meticulous and time-consuming analytical work is performed. By using the Q-XRMA software on pumices and scoriae of the 2019 Stromboli paroxysms, we have shown that precise identification and quantification of texturally and compositionally different rocks is possible.

Our study confirms that the proportion of scoria and pumice that can be observed at macroscale, and even thin section scale, is not a faithful estimator of the proportion of the two magma types feeding the eruptions. Micro-domains of rocks that have been initially identified as pumice and scoria based on textural characteristics, are in general not formed exclusively by LP or HP magmas, as they contain glasses with both shoshonitic-basaltic and shoshonitic compositions. The contribution of distinct magma types can be unambiguously observed even in texturally homogeneous samples, thanks to the application of this new image processing tool. In some cases,

10.1029/2022GC010774

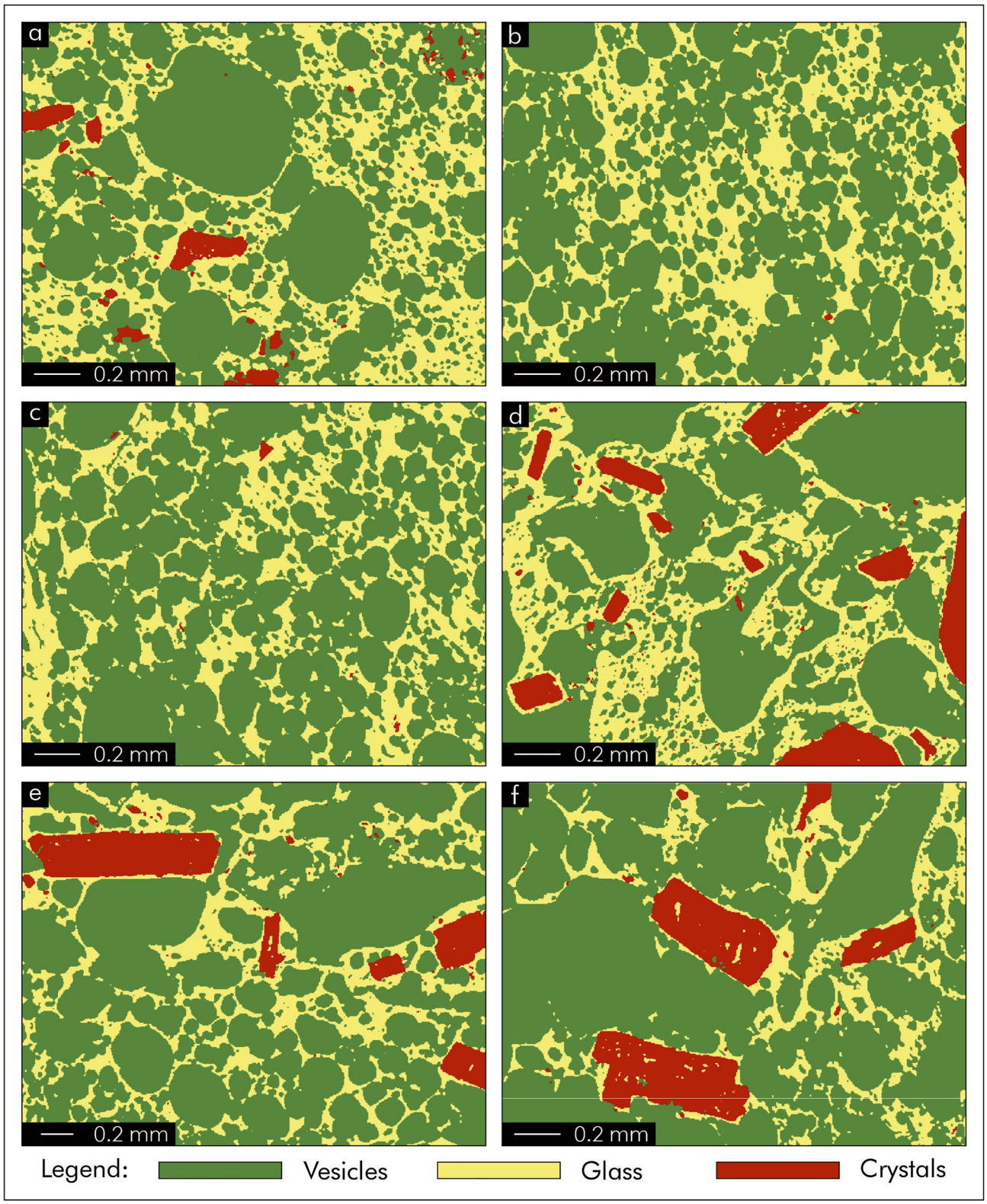

Figure 6. Results of the first cycle of the Quantitative X-Ray Map Analyzer for the micro-domains in product representative of the 3 July paroxysm: (a–c) phase maps of the constituents in pumice domains; and (d–f) phase maps of the constituents in scoria domains. (a) J_ST3_1; (b) J_ST5_1; (c) J_ST13_1; (d) J_ST7_2; (e) J_ST11_1; and (f) J_ST1_2.

10.1029/2022GC010774

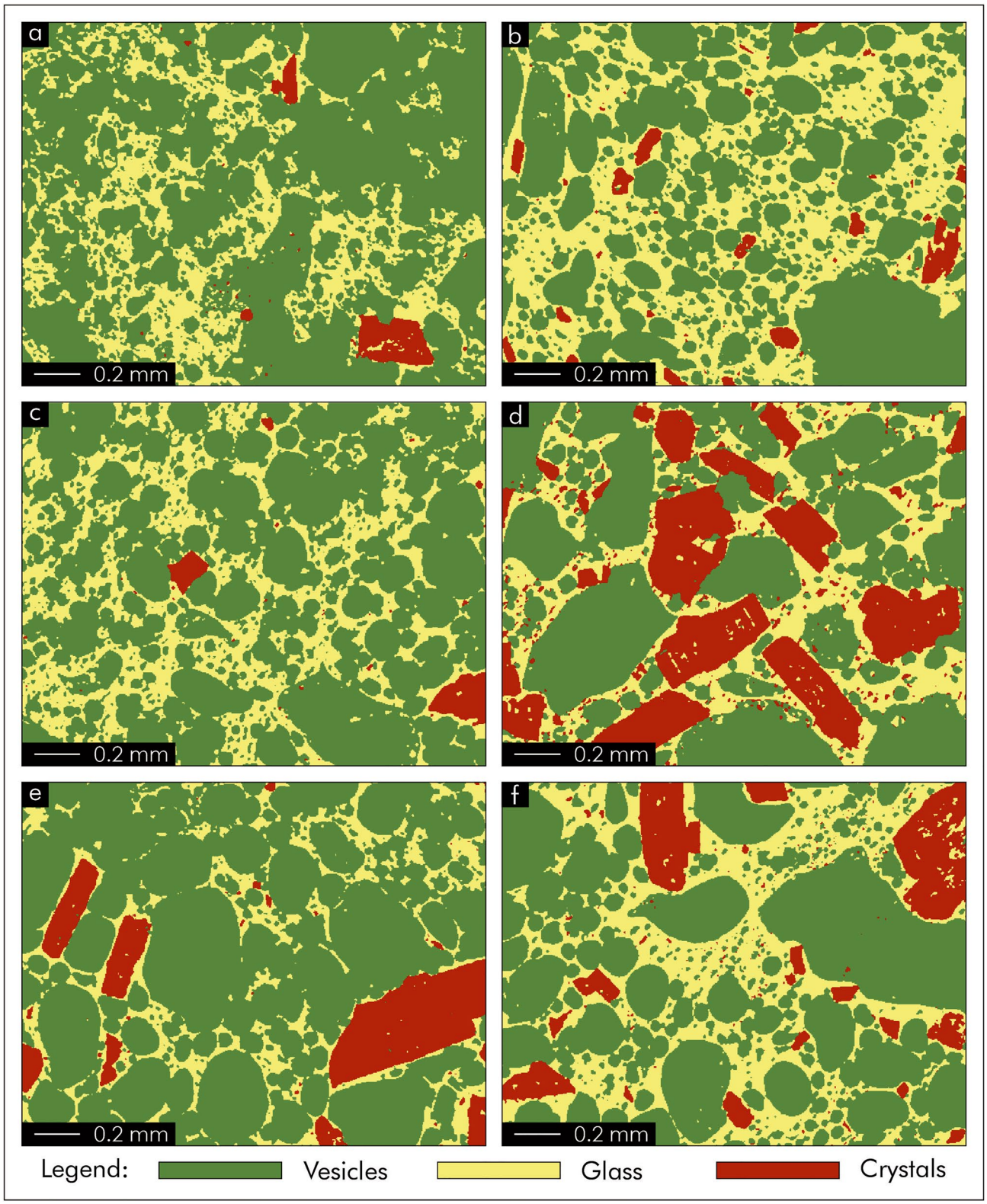

Figure 7. Results of the first cycle of the Quantitative X-Ray Map Analyzer for the micro-domains in product representative of the 28 August paroxysm: (a–c) phase maps of the constituents in pumice domains; and (d–f) phase maps of the constituents in scoria domains. (a) A_ST5_2; (b) A_ST9_1; (c) A_ST10_1; (d) A_ST2_1; (e) A_ST5_1; and (f) A_ST8_2.

10.1029/2022GC010774

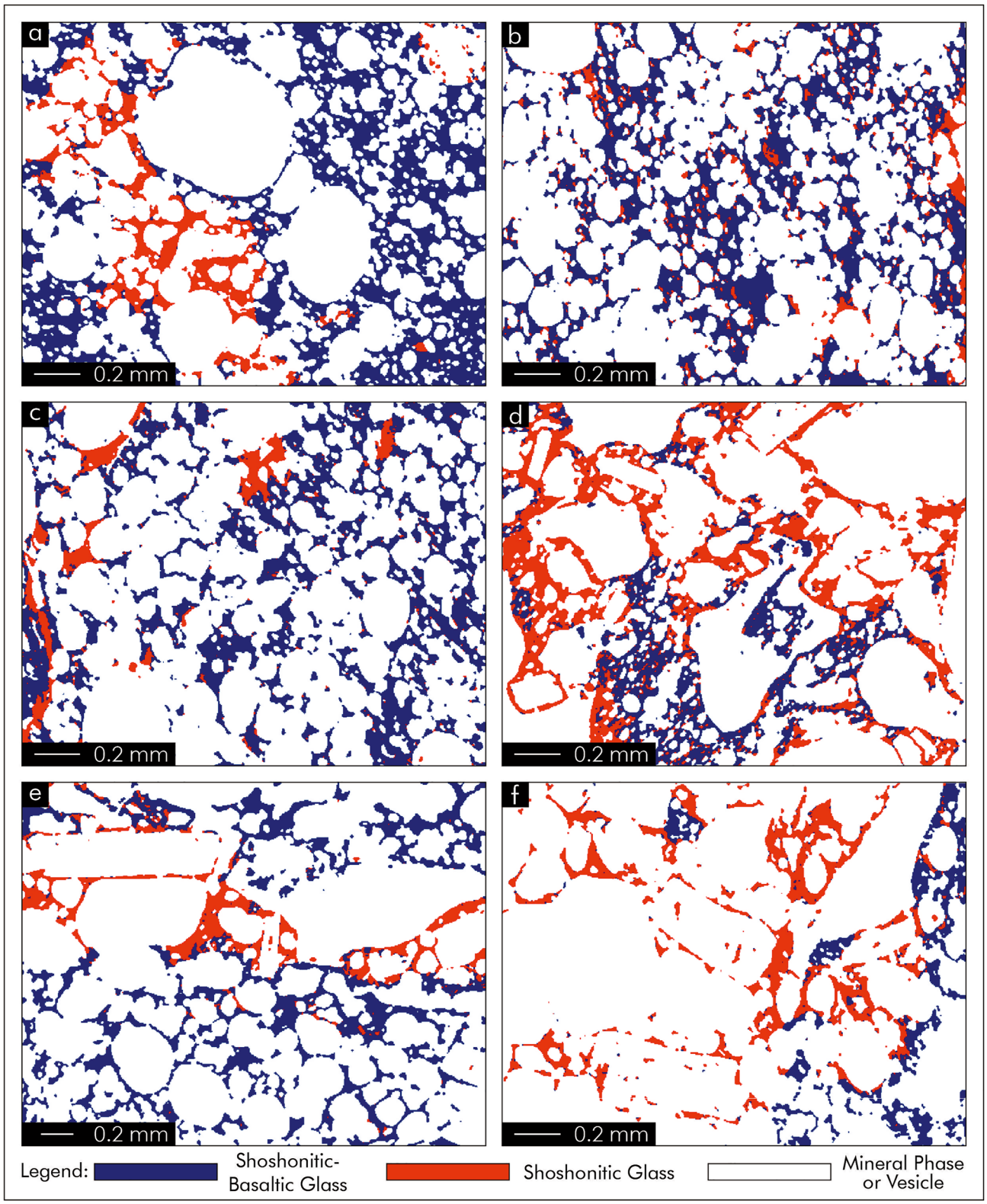

Figure 8. Results of the second cycle of the Quantitative X-Ray Map Analyzer on the glass fraction for the micro-domains in product representative of the 3 July paroxysm: (a–c) sub-phase distribution maps of the glass fraction in pumice domains; and (d–f) sub-phase distribution maps of the glass fraction in scoria domains. (a) J_ST3_1; (b) J_ST5_1; (c) J_ST13_1; (d) J_ST7_2; (e) J_ST11_1; and (f) J_ST1_2.

10.1029/2022GC010774

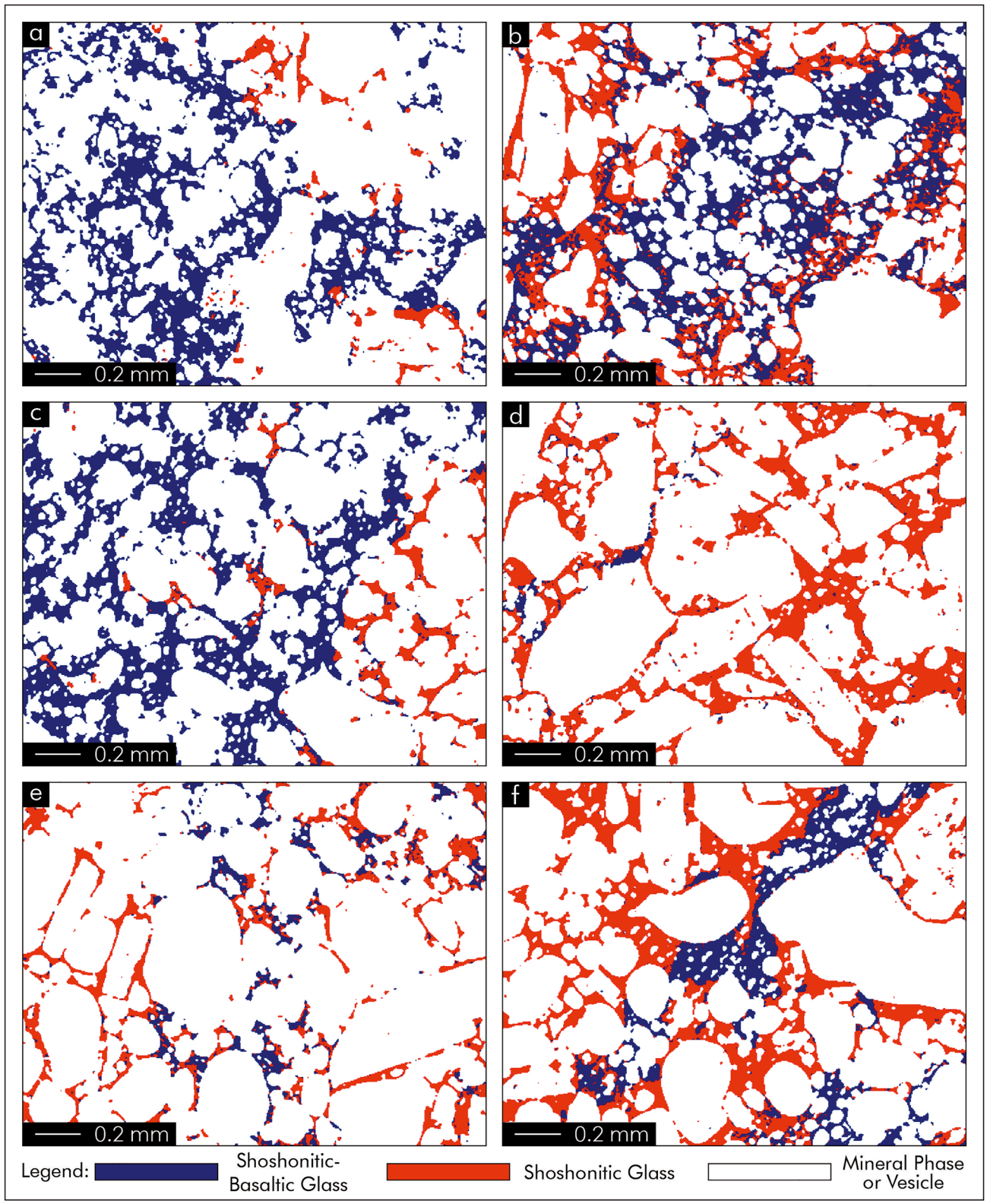

Figure 9. Results of the second cycle of the Quantitative X-Ray Map Analyzer on the glass fraction for the micro-domains in product representative of the 28 August paroxysm: (a–c) sub-phase distribution maps of the glass fraction in pumice domains; and (d–f) sub-phase distribution maps of the glass fraction in scoria domains. (a) A_ST5_2; (b) A_ST9_1; (c) A_ST10_1; (d) A_ST2_1; (e) A_ST5_1; and (f) A_ST8_2.

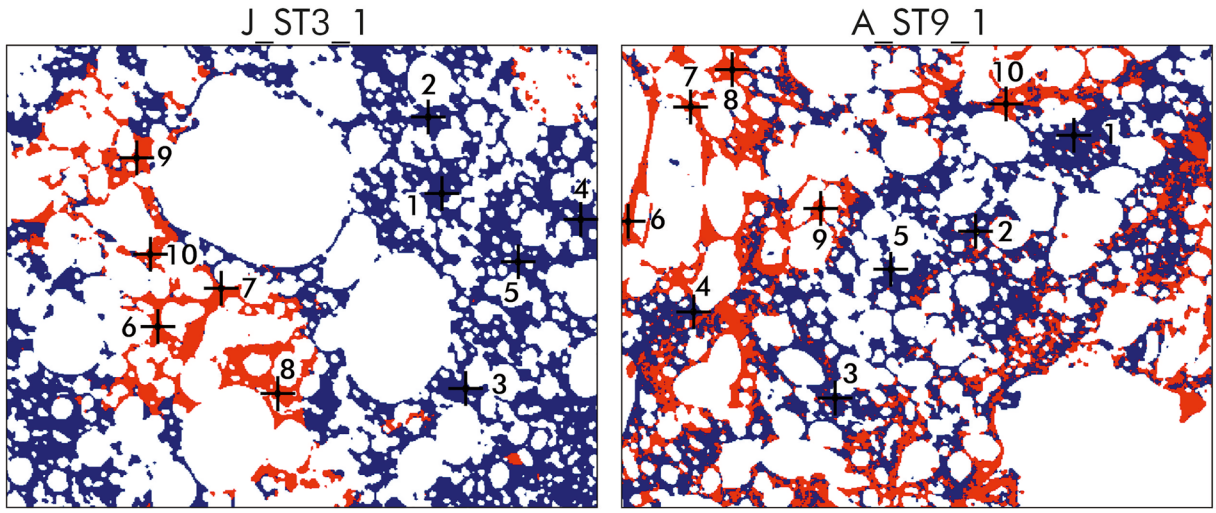

Domain	Analysis	Spots	SiO_2	TiO_2	Al_2O_3	FeO	MgO	CaO	Na_2O	K_2O
J_ST3_1	Mean Shoshonitic-Basaltic Glass	1-5	51.6	1.00	17.7	7.66	6.39	11.1	2.61	1.96
	Mean Shoshonitic Glass	6-10	55.2	1.68	15.5	9.26	3.65	7.11	3.27	4.31
A_ST9_1	Mean Shoshonitic-Basaltic Glass	1-5	52.1	1.07	17.5	7.76	5.99	10.7	2.59	2.30
	Mean Shoshonitc Glass	6-10	55.0	1.67	15.6	9.38	3.83	7.47	3.05	3.98

Figure 10. Position of the spot analyses collected in the shoshonitic-basaltic and shoshonitic glasses (blue and red areas, respectively) with the associated average major oxide concentrations.

severe discordances between the texture and composition typical of the pumice and scoria of Stromboli emerged. Bulk textural properties alone are often unable to fully capture the complexity and magnitude of the pre-eruptive interaction process when not in conjunction with in-depth chemical characterizations at the microscale. Furthermore, the quantitative results obtained through this study show there are subtle differences in the proportions of the two end-members constituting the products of the two investigated eruptions.

This study illustrates how the Q-XRMA software can be used as a starting point to parameterize textural and chemical features of volcanic rocks, which can be in turn useful for further specialized studies in the fields of petrology and volcanology.

Conflict of Interest

The authors declare no conflicts of interest relevant to this study.

Data Availability Statement

All the data used for the elaboration presented in this study are available as tables, Supporting Information S1 published in this work and as additional open-access data sets published at https://doi.org/10.5281/zenodo.7286364.

Acknowledgments
This work was supported by the funding program PIACERI 2020-22 of the University of Catania, project PAROSSISMA, code 22722132140 (Principal Investigator M. Viccaro). The authors are thankful to Marie Edmonds for her manuscript handling and the useful suggestions. Lucia Gurioli and the other three anonymous reviewers are also acknowledged for their important comments that greatly improved the early versions of the work.

References

Andronico, D., Corsaro, R. A., Cristaldi, A., & Polacci, M. (2008). Characterizing high energy explosive eruptions at Stromboli volcano using multidisciplinary data: An example from the 9 January 2005 explosion. *Journal of Volcanology and Geothermal Research*, *176*(4), 541–550. https://doi.org/10.1016/j.jvolgeores.2008.05.011

Andronico, D., Del Bello, E., D'Oriano, C., Landi, P., Pardini, F., Scarlato, P., et al. (2021). Uncovering the eruptive patterns of the 2019 double paroxysm eruption crisis of Stromboli volcano. *Nature Communications*, *12*(1), 4213. https://doi.org/10.1038/s41467-021-24420-1

Andronico, D., & Pistolesi, M. (2010). The November 2009 paroxysmal explosions at Stromboli. *Journal of Volcanology and Geothermal Research*, *196*(1–2), 120–125. https://doi.org/10.1016/j.jvolgeores.2010.06.005

Andronico, D., Taddeucci, J., Cristaldi, A., Miraglia, L., Scarlato, P., & Gaeta, M. (2013). The 15 March 2007 paroxysm of Stromboli: Video-image analysis, and textural and compositional features of the erupted deposit. *Bulletin of Volcanology*, *75*(7), 73. https://doi.org/10.1007/s00445-013-0733-2

Barberi, F., Rosi, M., & Sodi, A. (1993). Volcanic hazard assessment at Stromboli based on review of historical data. *Acta Vulcanologica*, *3*, 173–187. https://doi.org/10.1037/h0071325

Bertagnini, A., Di Roberto, A., & Pompilio, M. (2011). Paroxysmal activity at Stromboli: Lessons from the past. *Bulletin of Volcanology*, *73*(9), 1229–1243. https://doi.org/10.1007/s00445-011-04703

Bertagnini, A., Métrich, N., Francalanci, L., Landi, P., Tommasini, S., & Conticelli, S. (2008). Volcanology and magma geochemistry of the present day activity: Constraints on the feeding system. In S. Calvari, S. Inguaggiato, G. Puglisi, M. Ripepe, & M. Rosi (Eds.), *Learning from Stromboli*, *Geophysical Monograph Series* (Vol. 182, pp. 19–37). American Geophysical Union.

Bevilacqua, A., Bertagnini, A., Pompilio, M., Landi, P., Del Carlo, P., Di Roberto, A., et al. (2020). Major explosions and paroxysms at Stromboli (Italy): A new historical catalog and temporal models of occurrence with uncertainty quantification. *Scientific Reports*, *10*(1), 17357. https://doi.org/10.1038/s41598-020-74301-8

Corsaro, R. A., Miraglia, L., & Zanon, V. (2005). Petrologic monitoring of glasses in the pyroclastites erupted in February 2004 by the Stromboli Volcano, Aeolian Islands, Southern Italy. *Journal of Volcanology and Geothermal Research*, *139*(3–4), 339–343. https://doi.org/10.1016/j.jvolgeores.2004.08.002

Cossio, R., Borghi, A., & Ruffini, R. (2002). Quantitative modal determination of geological samples based on X-ray multielemental map acquisition. *Microscopy and Microanalysis*, *8*(2), 139–149. https://doi.org/10.1017/s1431927601020062

Coutelas, A., Godard, G., Blanc, P., & Person, A. (2004). Les mortiers hydrauliques: Synthèse bibliographique et premiers résultats sur des mortiers de Gaulle romaine. *Revue d'Archéométrie*, *28*(1), 127–139. https://doi.org/10.3406/arsci.2004.1068

Dainelli, N., Bonechi, F., Spagnolo, M., & Canessa, A. (2010). *Cartografia numerica: Manuale pratico per l'utilizzo dei GIS* (D. Flaccovio, Ed., p. 372).

Fazio, E., Ortolano, G., Visalli, R., Cirrincione, R., Fiannacca, P., Kern, H., et al. (2018). Strain rates of the syn-tectonic Symvolon pluton (Southern Rhodope Core Complex, Greece): An integrated approach combining quartz paleopiezometry, flow laws and PT pseudosections. *Italian Journal of Geosciences*, *137*(2), 219–237. https://doi.org/10.3301/IJG.2018.10

Francalanci, L., Tommasini, S., & Conticelli, S. (2004). The volcanic activity of Stromboli in the 1906–1998 period: Mineralogical, geochemical and isotope data relevant to the understanding of Strombolian activity. *Journal of Volcanology and Geothermal Research*, *131*(1–2), 179–211. https://doi.org/10.1016/S0377-0273(03)00362-7

Francalanci, L., Tommasini, S., Conticelli, S., & Davies, G. (1999). Sr isotope evidence for short magma residence time for the 20th century activity at Stromboli volcano, Italy. *Earth and Planetary Science Letters*, *167*(1–2), 61–69. https://doi.org/10.1016/S0012-821X(99)00013-8

Gardner, C. A., Cashman, K. V., & Neal, C. A. (1998). Tephra-fall deposits from the 1992 eruption of Crater Peak, Alaska: Implications of clast textures for eruptive processes. *Bulletin of Volcanology*, *59*(8), 537–555. https://doi.org/10.1007/s004450050208

Giordano, G., & De Astis, G. (2021). The summer 2019 basaltic Vulcanian eruptions (paroxysms) of Stromboli. *Bulletin of Volcanology*, *83*, 1. https://doi.org/10.1007/s00445-020-01423-2

Giudicepietro, F., López, C., Macedonio, G., Alparone, S., Bianco, F., Calvari, S., et al. (2020). Geophysical precursors of the July–August 2019 paroxysmal eruptive phase and their implications for Stromboli volcano (Italy) monitoring. *Scientific Reports*, *10*(1), 10296. https://doi.org/10.1038/s41598-020-67220-1

Gurioli, L., Colò, L., Bollasina, A. J., Harris, A. J. L., Whittington, A., & Ripepe, M. (2014). Dynamics of Strombolian explosions: Inferences from field and laboratory studies of erupted bombs from Stromboli volcano. *Journal of Geophysical Research: Solid Earth*, *119*(1), 319–345. https://doi.org/10.1002/2013JB010355

Hotelling, H. (1933). Analysis of a complex of statistical variables into principal components. *Journal of Educational Psychology*, *24*(6–7), 417–441. https://doi.org/10.1037/h0071325

Johnson, R. A., & Wichern, D. W. (1988). *Applied multivariate statistical analysis* (p. 607). Prentice-Hall.

Jolliffe, I. T. (2002). Principal component analysis. In *Springer series in statistics* (2nd ed.). Springer-Verlag. https://doi.org/10.1007/b98835

Karl Pearson, F. R. S. (1901). LIII. On lines and planes of closest fit to systems of points in space. *The London, Edinburgh, and Dublin Philosophical Magazine and Journal of Science*, *2*(11), 559–572. https://doi.org/10.1080/14786440109462720

Klug, C., & Cashman, K. V. (1994). Vesiculation of May 18, 1980, Mount St. Helens magma. *Geology*, *22*(5), 468–472. https://doi.org/10.1130/0091-7613(1994)022<0468:vommsh>2.3.co;2

Klug, C., Cashman, K. V., & Bacon, C. R. (2002). Structure and physical characteristics of pumice from the climactic eruption of Mount Mazama (Crater Lake), Oregon. *Bulletin of Volcanology*, *64*(7), 486–501. https://doi.org/10.1007/s00445-002-0230-5

Lanari, P., Vho, A., Bovay, T., Airaghi, L., & Centrella, S. (2019). Quantitative compositional mapping of mineral phases by electron probe micro-analyser. *Geological Society of London, Special Publication*, *478*(1), 39–63. https://doi.org/10.1144/SP478.4

Lanari, P., Vidal, O., De Andrade, V., Dubacq, B., Lewin, E., Grosch, E., & Schwartz, S. (2014). XMapTools: A MATLAB©-based program for electron microprobe X-ray image processing and geothermobarometry. *Computers & Geosciences*, *62*, 227–240. https://doi.org/10.1016/j.cageo.2013.08.010

Landi, P., Corsaro, R. A., Francalanci, L., Civetta, L., Miraglia, L., Pompilio, M., & Tesoro, R. (2009). Magma dynamics during the 2007 Stromboli eruption (Aeolian Islands, Italy): Mineralogical, geochemical and isotopic data. *Journal of Volcanology and Geothermal Research*, *182*(3–4), 255–268. https://doi.org/10.1016/j.jvolgeores.2008.11.010

Launeau, P., Cruden, A. R., & Bouchez, J. L. (1994). Mineral recognition in digital images of rocks: A new approach using multichannel classification. *The Canadian Mineralogist*, *32*(4), 919–933.

Leichter, A., Almeev, R. R., Wittich, D., Beckmann, P., Rottensteiner, F., Holtz, F., & Sester, M. (2022). Automated segmentation of olivine phenocrysts in a volcanic rock thin section using a fully convolutional neural network. *Frontiers of Earth Science*, *10*, 740638. https://doi.org/10.3389/feart.2022.740638

Li, Y., Onasch, M. C., & Guo, Y. (2008). GIS-based detection of grain boundaries. *Journal of Structural Geology*, *30*(4), 431–443. https://doi.org/10.1016/J.JSG.2007.12.007

Métrich, N., Bertagnini, A., & Di Muro, A. (2010). Conditions of magma storage, degassing and ascent at Stromboli: New insights into the volcano plumbing system with inferences on the eruptive dynamics. *Journal of Petrology*, *51*(3), 603–626. https://doi.org/10.1093/petrology/egp083

Métrich, N., Bertagnini, A., Landi, P., & Rosi, M. (2001). Crystallization driven by decompression and water loss at Stromboli volcano (Aeolian Islands, Italy). *Journal of Petrology*, *42*(8), 1471–1490. https://doi.org/10.1093/petrology/42.8.1471

Métrich, N., Bertagnini, A., Landi, P., & Rosi, M. (2005). Triggering mechanism at the origin of paroxysms at Stromboli (Aeolian Archipelago, Italy): The 5 April 2003 eruption. *Geophysical Research Letters*, *32*(10), L10305. https://doi.org/10.1029/2004GL022257

Métrich, N., Bertagnini, A., & Pistolesi, M. (2021). Paroxysms at Stromboli Volcano (Italy): Source, genesis and dynamics. *Frontiers of Earth Science*, *9*, 593339. https://doi.org/10.3389/feart.2021.593339

Neave, D. A., Buisman, I., & Maclennan, J. (2017). Continuous mush disaggregation during the long-lasting Laki fissure eruption, Iceland. *American Mineralogist*, *102*(10), 2007–2021. https://doi.org/10.2138/am-2017-6015CCBY

Ortolano, G., Visalli, R., Godard, G., & Cirrincione, R. (2018). Quantitative X-Ray Map Analyser (Q-XRMA): A new GIS-based statistical approach for Mineral Image Analysis. *Computers & Geosciences*, *115*, 56–65. https://doi.org/10.1016/j.cageo.2018.03.001

Ortolano, G., Zappalà, L., & Mazzoleni, P. (2014). X-Ray Map Analyzer: A new ArcGIS® based tool for the quantitative statistical data handling of X-ray maps (Geo- and material-science applications). *Computers & Geosciences*, *72*, 49–64. https://doi.org/10.1016/j.cageo.2014.07.006

Perugini, D., Ventura, G., Petrelli, M., & Poli, G. (2004). Kinematic significance of morphological structures generated by mixing of magmas: A case study from Salina Island (southern Italy). *Earth and Planetary Science Letters*, *222*(3–4), 1051–1066. https://doi.org/10.1016/j.epsl.2004.03.038

Pichavant, M., Di Carlo, M., Pompilio, M., & Le Gall, N. (2022). Timescales and mechanisms of paroxysm initiation at Stromboli volcano, Aeolian Islands, Italy. *Bulletin of Volcanology*, *84*(4), 36. https://doi.org/10.1007/s00445-022-01545-9

Pichavant, M., Pompilio, M., D'Oriano, C., & Di Carlo, I. (2011). Petrography, mineralogy and geochemistry of a primitive pumice from Stromboli: Implications for the deep feeding system. *European Journal of Mineralogy*, *23*(4), 499–517. https://doi.org/10.1127/0935-1221/2011/0023-2109

Pioli, L., Pistolesi, M., & Rosi, M. (2014). Transient explosions at open-vent volcanoes: The case of Stromboli (Italy). *Geology*, *42*(10), 863–866. https://doi.org/10.1130/g35844.1

Polacci, M. (2005). Constraining the dynamics of volcanic eruptions by characterization of pumice textures. *Annals of Geophysics*, *48*(4–5), 731–738.

Polacci, M., Arzilli, F., La Spina, G., Le Gall, N., Cai, B., Hartley, M. E., et al. (2018). Crystallisation in basaltic magmas revealed via in situ 4D synchrotron X-ray microtomography. *Scientific Reports*, *8*(1), 8377. https://doi.org/10.1038/s41598-018-26644-6

Polacci, M., Baker, D. R., Mancini, L., Favretto, S., & Hill, R. J. (2009). Vesiculation in magmas from Stromboli and implications for normal Strombolian activity and paroxysmal explosions in basaltic systems. *Journal of Geophysical Research*, *114*(B1), B01206. https://doi.org/10.1029/2008JB005672

Polacci, M., Baker, D. R., Mancini, L., Tromba, G., & Zanini, F. (2006). Three-dimensional investigation of volcanic textures by X-ray microtomography and implications for conduit processes. *Geophysical Research Letters*, *33*(13), L13312. https://doi.org/10.1029/2006GL026241

Pompilio, M., Bertagnini, A., Del Carlo, P., & Di Roberto, A. (2017). Magma dynamics within a basaltic conduit revealed by textural and compositional features of erupted ash: The December 2015 Mt. Etna paroxysms. *Scientific Reports*, *7*(1), 4805. https://doi.org/10.1038/s41598-017-05065-x

Richards, J. A., & Jia, X. (2006). *Remote sensing digital image analysis: An introduction* (p. 439). Springer-Verlag. https://doi.org/10.1007/3-540-29711-1

Roda, M., Zucali, M., Corti, L., Visalli, R., Ortolano, G., & Spalla, M. I. (2021). Blueschist mylonitic zones accommodating syn-subduction exhumation of deeply buried continental crust: The example of the Rocca Canavese Thrust Sheets Unit (Sesia–Lanzo Zone, Italian Western Alps). *Swiss Journal of Geosciences*, *114*(6), 1–33. https://doi.org/10.1186/s00015-021-00385-7

Rosi, M., Bertagnini, A., & Landi, P. (2000). Onset of persistent activity at Stromboli Volcano (Italy). *Bulletin of Volcanology*, *62*(4–5), 294–300. https://doi.org/10.1007/s004450000098

Rosi, M., Pistolesi, M., Bertagnini, A., Landi, P., Pompilio, M., & Di Roberto, A. (2013). Stromboli Volcano, Aeolian Islands (Italy): Present eruptive activity and hazards. *Geological Society, London, Memoirs*, *37*(1), 473–490. https://doi.org/10.1144/M37.14

Schiavi, F., Kobayashi, K., Moriguti, T., Nakamura, E., Pompilio, M., Tiepolo, M., & Vannucci, R. (2010). Degassing, crystallization and eruption dynamics at Stromboli: Trace element and lithium isotopic evidence from 2003 ashes. *Contributions to Mineralogy and Petrology*, *159*(4), 541–561. https://doi.org/10.1007/s00410-009-0441-2

Shea, T., Gurioli, L., & Houghton, B. F. (2012). Transitions between fall phases and pyroclastic density currents during the AD 79 eruption at Vesuvius: Building a transient conduit model from the textural and volatile record. *Bulletin of Volcanology*, *74*(10), 2363–2381. https://doi.org/10.1007/s00445-012-0668-z

Shea, T., Hellebrand, E., Gurioli, L., & Tuffen, H. (2014). Conduit- to localized-scale degassing during Plinian eruptions: Insights from major element and volatile (Cl and H_2O) analyses within Vesuvius AD 79 Pumice. *Journal of Petrology*, *55*(2), 315–344. https://doi.org/10.1093/petrology/egt069

Shea, T., Houghton, B. F., Gurioli, L., Cashman, K. V., Hammer, J. E., & Hobden, B. J. (2010). Textural studies of vesicles in volcanic rocks: An integrated methodology. *Journal of Volcanology and Geothermal Research*, *190*(3–4), 271–289. https://doi.org/10.1016/j.jvolgeores.2009.12.003

Sheldrake, T., & Higgins, O. (2021). Classification, segmentation and correlation of zoned minerals. *Computers & Geosciences*, *156*, 104876. https://doi.org/10.1016/j.cageo.2021.104876

Tarquini, S., & Favalli, M. (2010). A microscopic information system (MIS) for petrographic analysis. *Computers & Geosciences*, *36*(5), 665–674. https://doi.org/10.1016/j.cageo.2009.09.017

Trafton, K., & Giachetti, T. (2020). The morphology and texture of Plinian pyroclasts reflect their lateral sourcing in the conduit. *Earth and Planetary Science Letters*, *562*, 116844. https://doi.org/10.1016/j.epsl.2021.116844

Viccaro, M., Cannata, C., Cannavò, F., De Rosa, R., Giuffrida, M., Nicotra, E., et al. (2021). Shallow conduit dynamics fuel the unexpected paroxysms of Stromboli volcano during the summer 2019. *Scientific Reports*, *11*(1), 266. https://doi.org/10.1038/s41598-020-79558-7

Visalli, R., Ortolano, G., Godard, G., & Cirrincione, R. (2021). Micro-fabric analyzer (MFA): A new semiautomated ArcGIS-based edge detector for quantitative microstructural analysis of rock thin-sections. *ISPRS International Journal of Geo-Information*, *10*(2), 51. https://doi.org/10.3390/ijgi10020051

Yoshimura, S., Kuritani, T., Matsumoto, A., & Nakagawa, M. (2019). Fingerprint of silicic magma degassing visualised through chlorine microscopy. *Scientific Reports*, *9*(1), 786. https://doi.org/10.1038/s41598-018-37374-0

Yu, J., Wellmann, F., Virgo, S., von Domarus, M., Jiang, M., Schmatz, J., & Leibe, B. (2023). Superpixel segmentations for thin sections: Evaluation of methods to enable the generation of machine learning training data sets. *Computers & Geosciences*, *170*, 105232. https://doi.org/10.1016/j.cageo.2022.105232